

Article

# Monitoring the Spatiotemporal Trajectory of Urban Area Hotspots Using the SVM Regression Method Based on NPP-VIIRS Imagery

Yuling Ruan <sup>1,2</sup>, Yanhong Zou <sup>1,2,\*</sup>, Minghui Chen <sup>3</sup> and Jingya Shen <sup>1,2</sup>

<sup>1</sup> School of Geosciences and Info-Physics, Central South University, Changsha 410083, China; ry11996@csu.edu.cn (Y.R.); shenjingya1227@csu.edu.cn (J.S.)

<sup>2</sup> Key Laboratory of Metallogenic Prediction of Nonferrous Metals and Geological Environment Monitoring, Ministry of Education, Central South University, Changsha 410083, China

<sup>3</sup> Dongguan Geographic Information & Urban Planning Research Center, Dongguan 523129, China; 185011020@csu.edu.cn

\* Correspondence: zouyanhong@csu.edu.cn; Tel.: +86-139-7487-0863

**Abstract:** Urban area hotspots are considered to be an ideal proxy for spatial heterogeneity of human activity, which is vulnerable to urban expansion. Nighttime light (NTL) images have been extensively employed in monitoring current urbanization dynamics. However, the existing studies related to NTL images mainly concern detection of urban areas, leaving inner spatial differences in urban NTL luminosity poorly explored. In this study, we propose an innovative approach to explore the spatiotemporal trajectory of urban area hotspots using monthly Visible Infrared Imaging Radiometer Suite (VIIRS) NTL images. Firstly, multi-temporal VIIRS NTL intensity was decomposed by time-series analysis to obtain annual stable components after data preprocessing. Secondly, the support vector machine (SVM) regression model was utilized to identify urban area hotspots. In order to ensure the model accuracy, the grid search and cross-validation method was integrated to achieve the optimized model parameters. Finally, we analyzed the spatiotemporal migration trajectory of urban area hotspots by the center of gravity method (i.e., shift distance and angle of urban area hotspot centroid). The results indicate that our method successfully captured urban area hotspots with a regression coefficient over 0.8. Meanwhile, the findings give an intuitive understanding of coupling interaction between urban area hotspots and socioeconomic indicators. This study provides important insights for further decision-making regarding sustainable urban planning.

**Keywords:** urban area hotspot; nighttime light imagery; SVM regression; VIIRS; urbanization



**Citation:** Ruan, Y.; Zou, Y.; Chen, M.; Shen, J. Monitoring the Spatiotemporal Trajectory of Urban Area Hotspots Using the SVM Regression Method Based on NPP-VIIRS Imagery. *ISPRS Int. J. Geo-Inf.* **2021**, *10*, 415. <https://doi.org/10.3390/ijgi10060415>

Academic Editors: Wolfgang Kainz and Monika Sester

Received: 13 April 2021

Accepted: 4 June 2021

Published: 16 June 2021

**Publisher's Note:** MDPI stays neutral with regard to jurisdictional claims in published maps and institutional affiliations.



**Copyright:** © 2021 by the authors. Licensee MDPI, Basel, Switzerland. This article is an open access article distributed under the terms and conditions of the Creative Commons Attribution (CC BY) license (<https://creativecommons.org/licenses/by/4.0/>).

## 1. Introduction

Urbanization is a global concern associated with massive population shift, urban expansion, and industrial structure adjustment [1–3]. Especially as a developing country, China has experienced rapid urbanization since the reform and opening-up policy was implemented [4,5]. The rapid urban expansion led to intensive population increases and regional development differences. Therefore, timely and comprehensive understanding of urban growth is vital for sustainable urbanization. With advances in remote sensing and Geographic Information Systems (GIS) technology, satellite imagery provides convenient and spatially explicit ways of mapping urban expansion. Compared with other remote sensing products, the artificial nighttime light (NTL) image, as a recorder of anthropogenic luminosity [6–8], provides a more specific perspective of urban dynamics at different scales (i.e., local, regional, and global).

To date, two types of widely used types of NTL imagery at the global scale can be acquired from different satellite sensors: the Defense Meteorological Satellite Program/Operational Linescan System (DMSP/OLS) and the Visible Infrared Imaging Radiometer Suite (VIIRS) Day/Night Band (DNB) onboard the Suomi National Polar-Orbiting

Partnership (SNPP) satellite. These types of imagery have been increasingly exploited in studies of urbanization dynamics [9–12] and estimation of socioeconomic statistics [13–15]. In particular, the VIIRS images (2012–present), as an advanced NTL product, are superior to the former coarse-resolution DMSP/OLS (1992–2013) in many respects, for instance, higher spatial resolution (~500 m) and time resolution, without blooming and oversaturated pixels [16–18]. Furthermore, equipped with an onboard calibration system, the VIIRS images capture NTL intensity at a higher radiometric resolution than DMSP data [19–23]. Accordingly, there is a growing interest in taking advantage of VIIRS images in urban area extent extraction and socioeconomic estimation [24–29]. Due to the capacity of detecting lower light levels, raw VIIRS images contain some temporary light pixels and background noises; many studies have also focused on filtering algorithms or other processes to reduce the impact of noises. In addition to these studies, some researchers have paid attention to the relationship between urban NTL illumination and development disparity [30–32]. With the development of light emitting diode (LED) technology, the global transition to LED lights has not only allowed for an increase in light emission but also dramatically changed lighting spectra. Although, global spectral shift likely affects the ability of existing sensors such as DMSP and VIIRS to quantify artificial lights from space [16,17,33]. Given that they are not measuring incoming light in the blue band, the NTL illumination provides an intuitive approach to monitoring human activities.

From the view of nighttime lights, an urban area hotspot can be described as the region of nighttime light hotspot involving multiple bright pixels in an urban area as an ideal proxy of the area with intensified human activities [30,34], which can be regarded spatially as the urban center. NTL illumination mostly derives from artificial lights of urban areas, such as buildings, parking lots, and other elements of the built environment, which represent the level of urbanization development and are closely related to human activity. Therefore, the spatial distribution of NTL illumination intuitively reflects the regional spatial heterogeneity of urbanization [30]. Tracing urban-area hotspots not only reveals the reciprocity between urban expansion and human activities but also provides new insight into sustainable urbanization for government policymakers.

In recent years, some scholars have explored urban area hotspots using coarse-resolution DMSP NTL images. Xiao et al. [31] calculated centroids of urban agglomerations from NTL imagery and analyzed the dynamic shift of the centroids. Zhao et al. [32] studied the spatial differentiation and morphologic characteristics of urban core zones in China based on geomorphologic partition theory. Cai et al. [34] identified the structure of polycentric cities using multi-source geospatial big data. In addition, Zheng et al. [30] utilized the Gaussian volume model to depict urban NTL hotspot features quantitatively. Nevertheless, studies regarding identification of urban area hotspots by VIIRS images have not been reported. Given the superiority of satellite sensors, the VIIRS image is more sensitive in detecting low and high NTL intensity [35,36], which offers the possibility to identify urban area hotspots from the perspective of a good data source. However, due to the differences in city size and urban expansion pattern, the spatial distribution of VIIRS NTL intensity is not always suitable for the Gaussian volume model. Therefore, it is necessary to find a universal approach to identify the polycentric urban area hotspots.

The Support Vector Machine (SVM) method proposed by Vapnik [37] is a promising machine learning technique describing the nonlinear relationship between model inputs and outputs with good generalization ability [38]. It has been increasingly used in remote sensing applications as classifier or regression models [39–42]. The SVM regression model serves as a sample statistical theory which can be used for function fitting for scattered points in the transformation space by a generalized linear function. Thus, it is expected to obtain a continuous prediction output. For instance, Zhan et al. [43] and Yang et al. [44] utilized the SVM regression model to depict urban heat islands (UHI). The UHI is a phenomenon that occurs in urban areas and is associated with significantly higher ambient temperature within a city compared to the surrounding non-urban area. In contrast, an urban area hotspot represents a region that includes a substantial number of lit pixels with

higher NTL intensity. We will employ the SVM regression method to investigate the urban area hotspots due to the similarities between the spatial characteristics of UHI and urban area hotspots.

In this study, we designed a practicable framework to explore the space-time dynamics of urban area hotspots by monthly VIIRS NTL data. The primary objectives of our study were as follows: (1) to identify the urban area hotspots by using the SVM regression model, and (2) to analyze the spatiotemporal trajectory of the urban area hotspots.

## 2. Study Area and Datasets

### 2.1. Study Area

Wuhan ( $29^{\circ}58' - 31^{\circ}22' N$ ,  $113^{\circ}41' - 115^{\circ}05' E$ ), the capital city of Hubei province and the largest city in central China, plays a crucial part in the economy, industry, and transportation of the whole country. Wuhan is located in the eastern part of Jiangnan plain and has a total land area of  $8569.15 \text{ km}^2$  divided among 13 municipal districts (Jiangnan, Jiangxia, Qiaokou, Jiang'an, Huangpi, Xinzhou, Hongshan, Wuchang, Hanyang, Caidian, Hannan, Dongxihu, Qingshan) (Figure 1). Over recent years, Wuhan has grown to a total population and urban built-up area of 10.22 million and  $534.28 \text{ km}^2$  in 2013, and 11.08 million and  $723.74 \text{ km}^2$  in 2018, respectively. The rapid urbanization in Wuhan resulted in a striking increase in artificial light illumination from 2013 to 2018. Thus, Wuhan is regarded as a suitable area for our study.

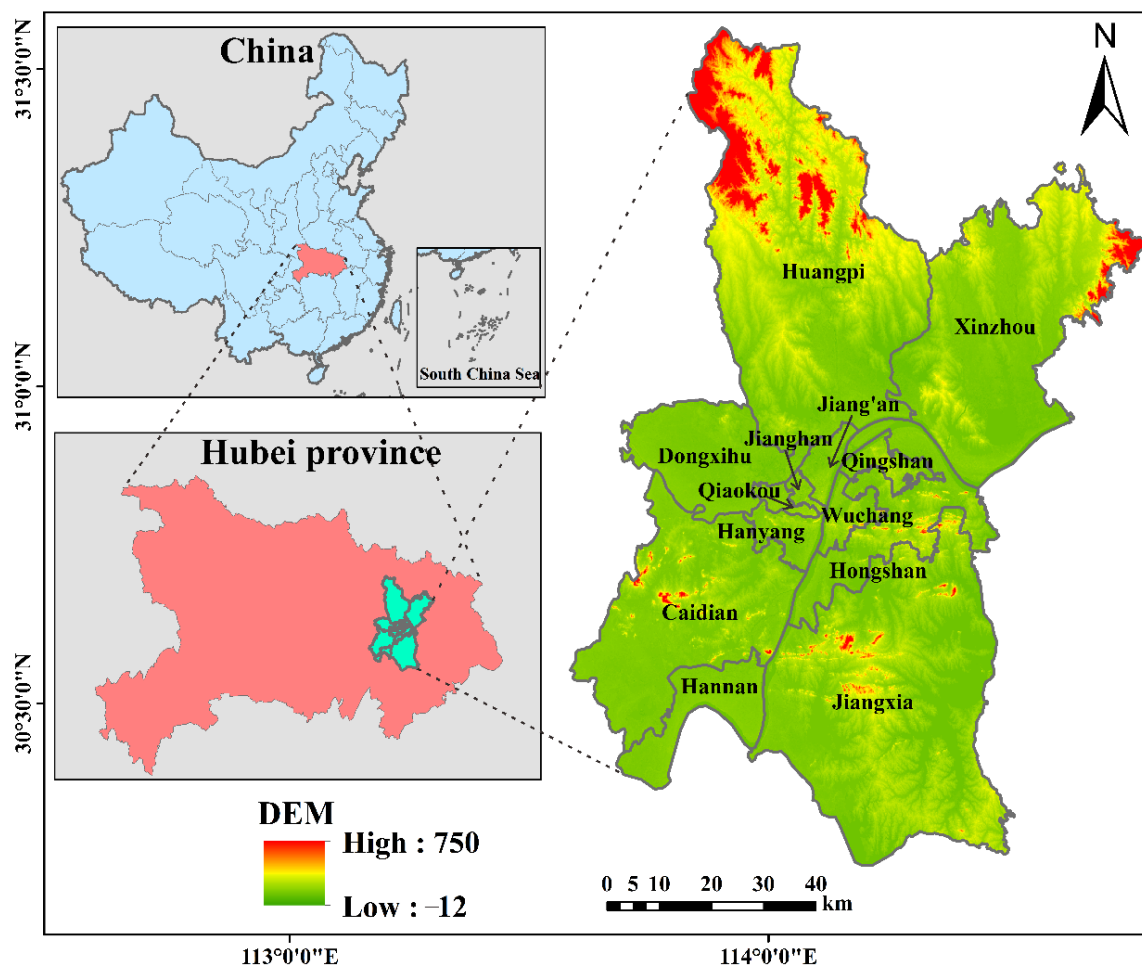


Figure 1. Location of the study area, municipal districts of Wuhan, Hubei in China.

## 2.2. Nighttime Light Data and Preprocessing

Monthly VIIRS NTL images for 70 months from January 2013 to December 2018 were acquired from NOAA/NGDC ([http://ngdc.noaa.gov/eog/viirs/download\\_viirs\\_ntl.html](http://ngdc.noaa.gov/eog/viirs/download_viirs_ntl.html) accessed on 1 June 2020) (see Table 1). Two versions of monthly composite VIIRS products, the “vcm” (any data impacted by stray light were excluded) and “vcmsl” (stray light-impacted data were corrected) data, were used in this study. The preprocessing of monthly VIIRS images involved the following three steps [26]: (1) since the monthly VIIRS NTL imagery is an initial product containing lit pixels from cities, towns, and other luminous sources, the annual “vcm-orm-ntl” composite of 2015 was utilized to filter temporary light pixels and background noises. In addition, given the unavailability of the “vcm” and “vcmsl” data in June 2018, we used the corresponding data in June 2017 to represent them. (2) All zero values in the “vcm” data were replaced by “vcmsl” data from the corresponding month to gain more reliable monthly VIIRS data. Subsequently, a Savitzky–Golay (SG) filter was adopted to remove abnormal observations in sequential monthly VIIRS NTL data while retaining their overall trends. It is a smoothing algorithm based on local polynomial least-squares fitting [45], which has been extensively applied in time-series analysis of remote sensing imagery [46,47]. (3) All preprocessed monthly VIIRS NTL images were re-projected to the Asia\_North\_Albers\_Equal\_Area\_Conic projection and resampled at 480 m. The preprocessed datasets were used to generate annual stable VIIRS NTL data by quantifying the temporal changes of VIIRS NTL brightness based on the time-series analysis method (Section 3.1).

**Table 1.** Two versions of available monthly VIIRS images, vcm (any data impacted by stray light were excluded) and vcmsl (stray light-impacted data were corrected) during 2013–2018.

NTL Data	2013		2014		2015		2016		2017		2018	
	vcm	vcmsl										
January	✓	✓	✓	✓	✓	✓	✓	✓	✓	✓	✓	✓
February	✓	✓	✓	✓	✓	✓	✓	✓	✓	✓	✓	✓
March	✓	✓	✓	✓	✓	✓	✓	✓	✓	✓	✓	✓
April	✓	✓	✓	✓	✓	✓	✓	✓	✓	✓	✓	✓
May	✓	✓	✓	✓	✓	✓	✓	✓	✓	✓	✓	✓
June	✓	✓	✓	✓	✓	✓	✓	✓	✓	✓	/	/
July	✓	✓	✓	✓	✓	✓	✓	✓	✓	✓	✓	✓
August	✓	✓	✓	✓	✓	✓	✓	✓	✓	✓	✓	✓
September	✓	✓	✓	✓	✓	✓	✓	✓	✓	✓	✓	✓
October	✓	✓	✓	✓	✓	✓	✓	✓	✓	✓	✓	✓
November	✓	✓	✓	✓	✓	✓	✓	✓	✓	✓	✓	✓
December	✓	✓	✓	✓	✓	✓	✓	✓	✓	✓	✓	✓

## 2.3. Auxiliary Data

In contrast to traditional statistical survey data, point of interest (POI) data provides a more precise location-based representation of urban spatial characteristics related to human activities. Therefore, POI data were used to explore the correlation between the spatial distribution of hotspots and POIs. In our research, a total of 328,803 POIs from Wuhan in 2018 were obtained using Baidu Map, which consisted of more than 15 types of artificial surface features, such as restaurants, schools, residences, cinema, shopping, and parks (Figure 2). A kernel density analysis of POIs in the study area can identify the location of the city center, the higher degree of aggregation of POIs indicating more-intensive human activities. It can be used as a valuable reference for urban area hotspots.

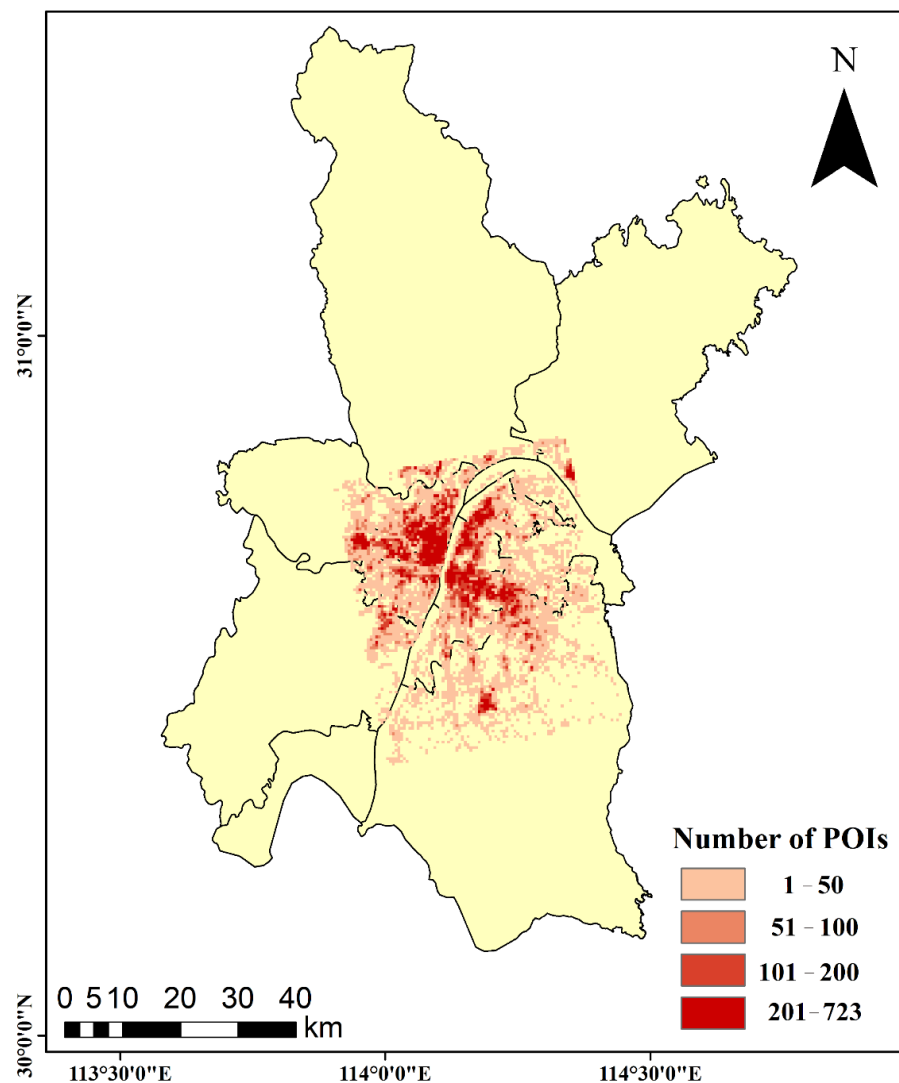


Figure 2. POIs of Wuhan in 2018 at the pixel scale.

To ensure the consistency of geographic coordinate systems, we further converted the coordinates of POI to Asia\_North\_Albers\_Equal\_Area\_Conic projected coordinates. Kernel density analysis was conducted to generate a POI density map to further validate our method for identifying urban area hotspots.

Considering the effects of urbanization on urban area hotspots, we selected a built-up urban area and socioeconomic statistics (i.e., population and GDP) as indicators to quantitatively explore the interaction between urban hotspots variation and economic statistics. The socioeconomic indicators from 2013 to 2018 were obtained from the Wuhan statistical yearbook from the Wuhan Bureau of Statistics (<http://tjj.wuhan.gov.cn/tjfw/tjnj>, accessed on 1 June 2020). Due to a lag in statistical data, the Wuhan statistical yearbook 2014 reflected the socioeconomic status of Wuhan city in 2013. Because the Wuhan statistical yearbook 2019 was not available, we used the statistics data obtained from Wuhan statistical yearbook 2018 to represent not only 2017 but also 2018.

### 3. Methodology

The methods used in this study included the following three steps: data processing of monthly VIIRS images, SVM regression modeling for urban area hotspot identification, and spatiotemporal trajectory analysis of urban area hotspots (Figure 3).

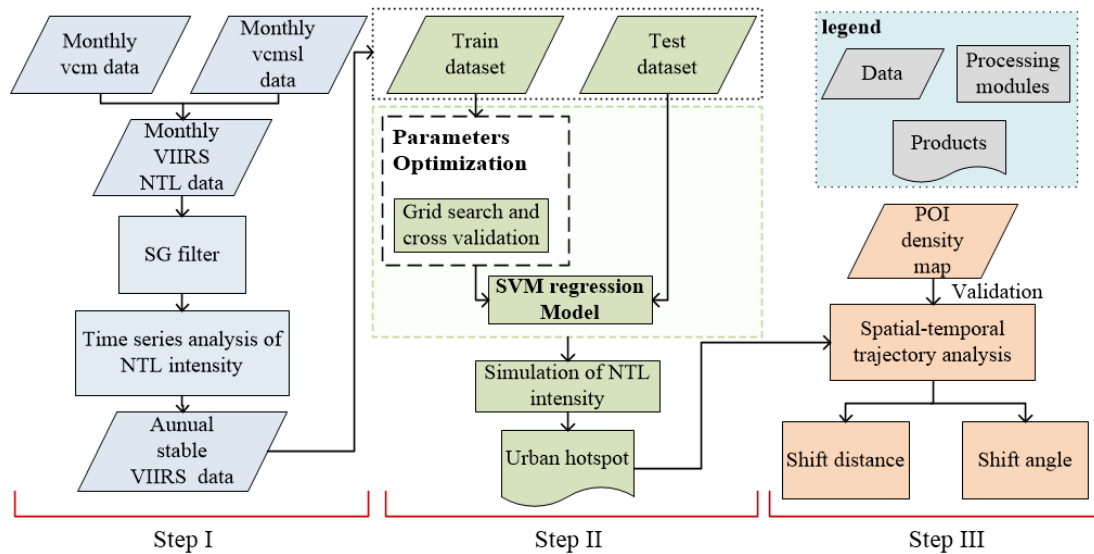


**Figure 3.** Flowchart of our proposed application framework.

Above all, given the unavailability of annual VIIRS NTL images each year, time-series analyses were conducted on monthly VIIRS images to obtain stable annual VIIRS images. Then, we divided the stable annual NTL pixel intensities for each year into a training set and testing set for training and validating the SVM regression model for identification of urban area hotspots. To ensure the accuracy and robustness of our SVM regression model, grid search and cross-validation were combined to retrieve the optimal parameters. Finally, the space-time trajectory of the centroid of the urban area hotspot was depicted by the differential distance and angle to reveal its spatiotemporal dynamics. The specific details of our proposed procedures are described in the following sections.

### 3.1. Time-Series Analysis of VIIRS NTL Intensity

Previous studies demonstrated the existence of monthly variation of VIIRS NTL intensity [48,49]. The NTL brightness is extremely sensitive to the influence of land surface albedo change, showing a regular fluctuation during a year. To identify the urban NTL hotspots accurately, we needed to obtain the annual stable component of VIIRS data (annual stable VIIRS data) by the time-series analysis method for 12 monthly VIIRS images. The seasonal variation of NTL intensity was quantified using Equation (1) [26]:

$$NTL_{it} = NTL_{stable} + a_1 \cos\left(\frac{2\pi}{T}t\right) + a_2 \sin\left(\frac{2\pi}{T}t\right) \quad (1)$$

where  $NTL_{it}$  represents the time-series observations of NTL intensity of a pixel for month  $it$ ,  $NTL_{stable}$  refers to annual stable NTL data, and  $T$  denotes 12 months of one year.

Considering the possible existing phenomenon of pixel-level NTL intensity seasonal variation, we performed the curve fitting of seasonal variations test for 2013. As illustrated in Figure 4, the test achieved a good performance at the pixel scale, with a high goodness of fit ( $R^2$ ). The  $R^2$  values for the intra-city pixels (Figure 4a–d) in Wuhan in 2013 were above 0.85, indicating a more apparent NTL intensity seasonality in urban areas. Obviously, the time-series analysis model can capture the general trend of monthly VIIRS NTL intensity and remove the influence of seasonal variation effectively from the observed NTL radiance intensity. Using the time-series analysis method, we obtained reliable annual stable NTL data during 2013–2018. The NTL intensity of annual stable NTL data were split into training sets and test sets for further identifying urban area hotspots using the machine learning method of SVM [43,44].

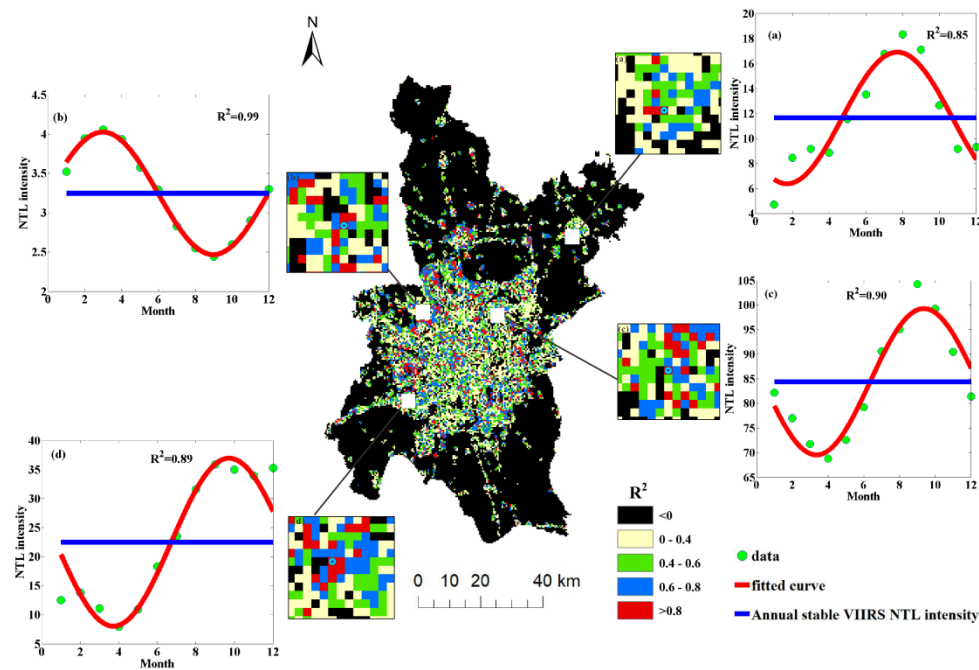


**Figure 4.** Observed seasonal variation of NTL intensity at the pixel scale from Wuhan in 2013: (a–d) curve-fitted of four different pixels’ seasonal variation.

### 3.2. SVM Regression Model

As a machine learning method, the support vector machine (SVM) method has achieved good results in nonlinear regression model fitting [50,51]. The Gaussian radial basis function (RBF) kernel has been generally utilized for the optimal SVM solution for its advantage of nonlinear mapping [52]. Therefore, we employed the SVM regression model with RBF kernel function to identify Wuhan’s urban area hotspots from 2013 to 2018 in this study.

The basic theory of SVM regression is demonstrated as follows. Given the form of training data  $(x_i, y_i)$ ,  $x_i$  represents the training vectors and  $y_i$  denotes their target values. Supposing that the linear regression function is  $f(x) = W^T \cdot x + b$ , the SVM method can be transformed into searching for the extreme value with the following equations:

$$\min \frac{1}{2} \|w\|^2 + C \sum_{i=1}^p (\xi_i + \xi_i^*) \quad (2)$$

$$\begin{cases} f(x_i) - y_i \leq \xi_i^* + \varepsilon_i, \\ f(x_i) - y_i \leq \xi_i + \varepsilon_i, & i = 1, \dots, p \\ \xi_i, \xi_i^* \geq 0, \end{cases} \quad (3)$$

where  $W$  represents the weight vector,  $C$  denotes regularization constant,  $\xi_i, \xi_i^*$  are positive slack variables, and  $\varepsilon$  is the parameter of the  $\varepsilon$ -intensive objective function. The Lagrange multiplier method was used to transform the original problem into a dual problem. After solving the dual problem, the fitting function can be simplified as

$$f(x) = \sum_{i=1}^p (m_i - m_i^*) k(x, x_i) + n \quad (4)$$

where  $m_i$  and  $m_i^*$  are the corresponding support vectors of samples and  $k(x, x_i)$  represents the kernel function.

Specifically, the SVM regression model has two significant parameters, the penalty parameter  $C$  and kernel coefficient  $\gamma$ . The choice of an appropriate model parameter influences the regression performance directly. As an essential tool for parameter optimization,

the grid search method can thoroughly search until the acquisition of model-optimized parameters. In addition, the partition of the training data also impacts the evaluation results of the parameter combination. Therefore, grid search and k-fold cross-validation (K-CV) methods have been combined to reduce the training error caused by sampling randomness and ensure the accuracy of the model [53].

Referring to Zhan et al. [43] and Yang et al., [44], the SVR model with RBF kernel function can effectively build the non-linear relationship between geographic coordinate vector (longitude and latitude) and surface urban heat island intensity. Therefore, the longitude and latitude served as the inputs of SVR to build the NTL intensity prediction model in this study. The initial  $C$  and  $\gamma$  ranged from  $2^{-15}$  to  $2^{15}$ , and the step interval was 1. To perform a five-fold CV method, the input dataset was divided into five subsets for SVM regression. Consequently, based on annual stable VIIRS data using the SVM regression algorithm, we obtained the urban area hotspots of Wuhan in 2013, 2015, and 2018.

### 3.3. Spatiotemporal Migration Analysis of Urban Area Hotspot

The morphology of urban area hotspots exhibits different shapes and magnitudes, making it difficult to separately analyze cluster dynamics for each urban area hotspot. Therefore, to explore the relationship between urban area hotspots and socioeconomic indicators, this study adopted the center of gravity method to analyze the spatiotemporal migration patterns of urban area hotspots from the perspective of the whole study area. Over the selected years, the shift of the gravity center reveals the variation of NTL illumination intensity with urbanization level, thereby reflecting the spatial heterogeneity of human activity. The position of the gravity center of the urban area hotspot was calculated as follows:

$$X_t = \frac{\sum_{i=1}^n (C_{ti} \times X_i)}{\sum_{i=1}^n C_{ti}} \quad (5)$$

$$Y_t = \frac{\sum_{i=1}^n (C_{ti} \times Y_i)}{\sum_{i=1}^n C_{ti}} \quad (6)$$

where  $X_t$  and  $Y_t$  represent the longitude and latitude of the gravity center of an urban area hotspot at time  $t$ , respectively;  $X_i$  and  $Y_i$  denote the longitude and latitude of the urban area hotspot at the  $i$ th pixel scale, respectively;  $C_{ti}$  is the NTL radiance intensity of the  $i$ th pixel at time  $t$ .

Additionally, the shift distance ( $L$ ) and angle ( $\alpha$ ) of the gravity center were calculated by Equations (7) and (8), respectively. The magnitude of shift distance indicates the urban expansion intensity during different periods, and the shift angle reveals the main directions of urban expansion.

$$L_{t+1} = \sqrt{(x_{t+1} - x_t)^2 + (y_{t+1} - y_t)^2} \quad (7)$$

where  $L_{t+1}$  represents the shift distance of the gravity center of the urban area hotspot in the period  $t-t+1$ .

$$\alpha_{t+1} = \begin{cases} \arctan\left\{\frac{y_{t+1}-y_t}{x_{t+1}-x_t}\right\} & x_{t+1} \geq x_t, y_{t+1} \geq y_t \\ \pi - \arctan\left\{\frac{y_{t+1}-y_t}{x_{t+1}-x_t}\right\} & x_{t+1} < x_t, y_{t+1} \geq y_t \\ \pi + \arctan\left\{\frac{y_{t+1}-y_t}{x_{t+1}-x_t}\right\} & x_{t+1} < x_t, y_{t+1} < y_t \\ 2\pi + \arctan\left\{\frac{y_{t+1}-y_t}{x_{t+1}-x_t}\right\} & x_{t+1} \geq x_t, y_{t+1} < y_t \end{cases} \quad (8)$$

where  $\alpha_{t+1}$  denotes the shift angle of the gravity center of the urban area hotspot from  $t$  to  $t+1$ .

## 4. Results

### 4.1. Nighttime Light Data Processing

Figure 5 shows monthly VIIRS images (Figure 5a–l) and annual stable images (Figure 5m) for Wuhan in 2013. The observed monthly VIIRS NTL intensity exhibits apparent seasonality at the city scale (Figure 6a) and pixel scale (Figure 6b), which is mainly influenced by the

seasonally changed albedo. In the winter, snowfall significantly increased and vegetation decreased, leading to an increase of NTL brightness. In the summer, increased vegetation resulted in a decrease in NTL illumination.

As Figure 7 illustrates, the pixels in urban areas have clear seasonal variations during 2013–2018. In contrast, background (non-urban area) pixels are not correlated with the seasons. This is because the albedo of land surface shows more apparent and regular changes in the urban areas than those in the non-urban areas. We also calculated the Pearson correlation coefficient between annual stable VIIRS data in 2015 and annual “vcm-orm-ntl” composite data of 2015. A high correlation (0.98) was obtained, which supports the validity of the annual stable VIIRS data after taking seasonal variations into consideration.

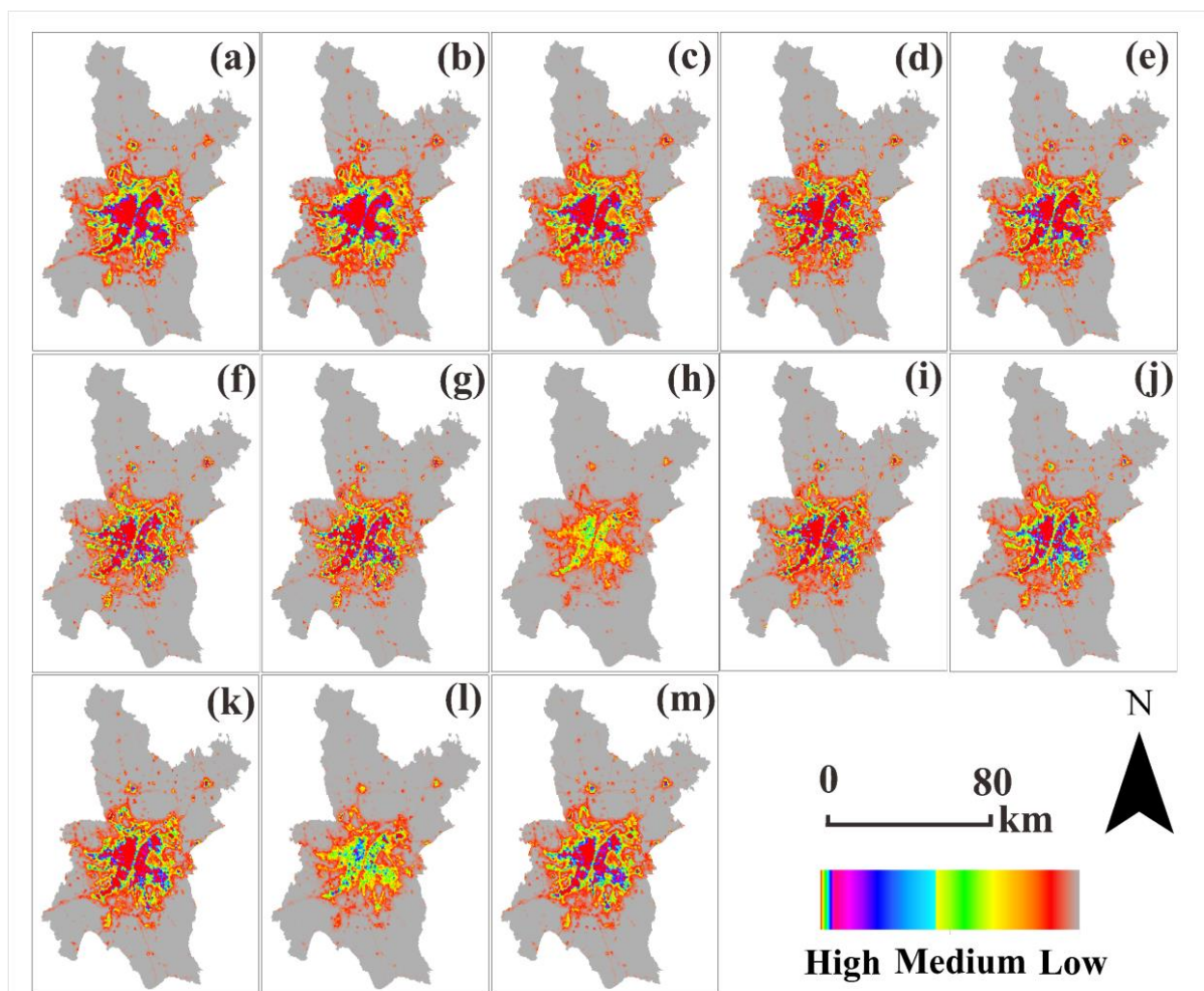


**Figure 5.** Monthly VIIRS images and annual stable images for Wuhan in 2013: (a) annual stable VIIRS data; (b–m) monthly images from January to December.

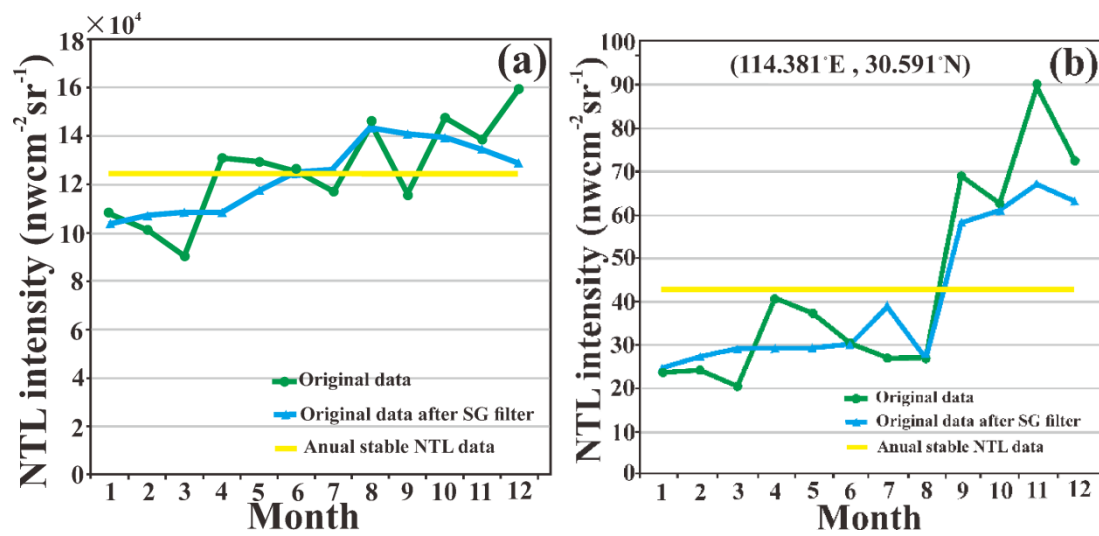


**Figure 6.** Temporal variations of Wuhan city in 2013: (a) temporal variation of NTL intensity at the city scale; (b) temporal variation of NTL intensity at the pixel scale.

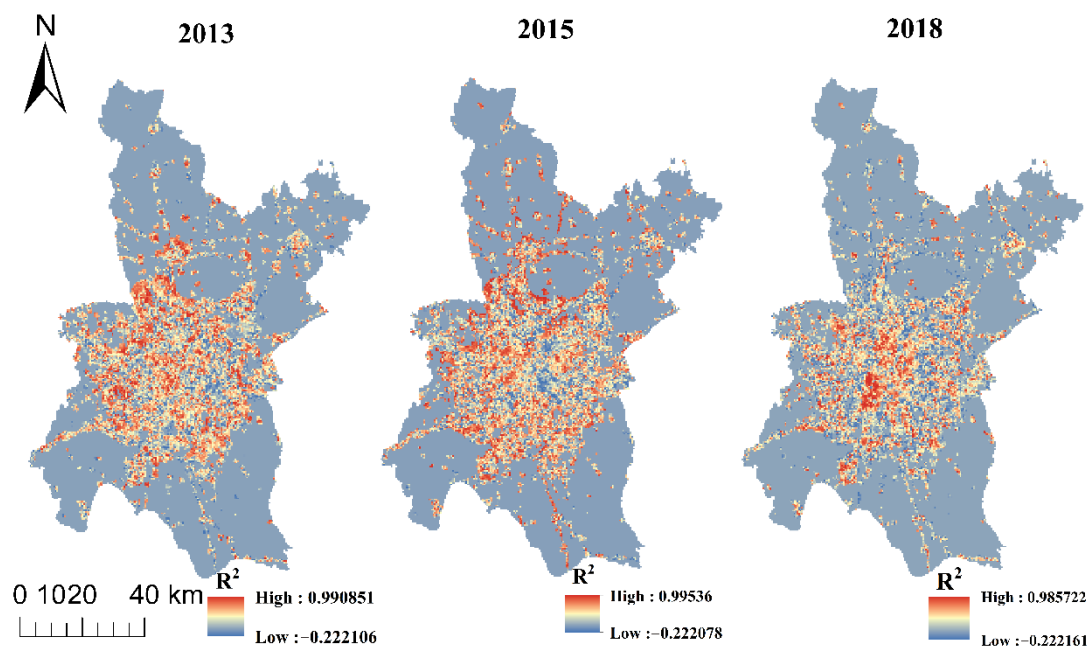


**Figure 7.** Seasonal variations in Wuhan at the pixel scale during 2013–2018.

To verify the performance of seasonal curve fitting, linear regression analyses of pixel-level VIIRS NTL intensity between winter and spring (Figure 8a), summer (Figure 8b), and autumn (Figure 8c) were conducted separately. Specifically, we used the average VIIRS NTL intensity in March–May, June–August, September–November, and December–February to represent spring, summer, autumn, and winter, respectively. As Figure 8 demonstrates, a fairly good linear relationship of NTL intensity between winter and the other seasons (spring, summer, autumn) was observed, with a slope close to 1. They all show a high correlation ( $R^2 > 0.9$ ), with a p-value of  $< 0.01$ . The results show that seasonal curve fitting can effectively reduce the impact of the seasonal variation of NTL illumination.

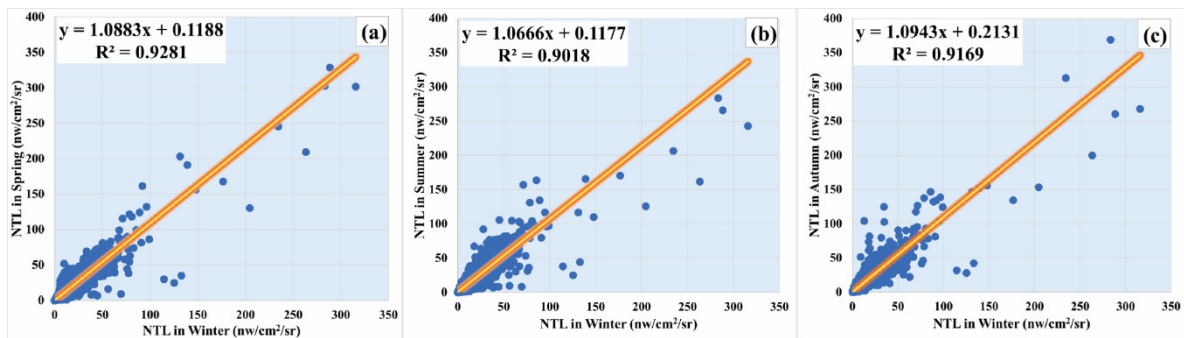


**Figure 8.** Linear relationship of filtered NTL intensity between winter and the other three seasons at the pixel scale: (a) spring–winter; (b) summer–winter; (c) autumn–winter.

Figure 9 reveals the increment of NTL brightness ( $NTL_{Inc}$ ) from 2013 to 2018 in Wuhan at the pixel scale. The NTL intensity of new urban areas (i.e., Hannan, Huangpi, and Caidian municipal districts) increased more than that of the old ones (i.e., Wuchang and Jiang'an municipal districts), indicating more rapid urbanization in emerging urban areas compared to old towns. Emerging urban clusters experienced a relatively high NTL increase during the period, as high as  $270 \text{ nWcm}^{-2}\text{sr}^{-1}$ . The positive relationship between NTL increase and population growth indicates that population growth in Wuhan made a contribution to the increase of urban NTL intensity during 2013–2018. Figure 9b,c shows the district-scale relationship between the total population growth and total  $NTL_{Inc}$ , and the GDP growth per capita and mean  $NTL_{Inc}$ , respectively. We have detected the possible noise of data (such as big outliers) according to the Pauta criterion ( $3\sigma$  criterion) [54]. The result reveals that all data points are within the allowable error range; thus, the obtained linear regression model is acceptable. There is a certain positive correlation between NTL growth, on the one hand, and GDP and population, on the other.

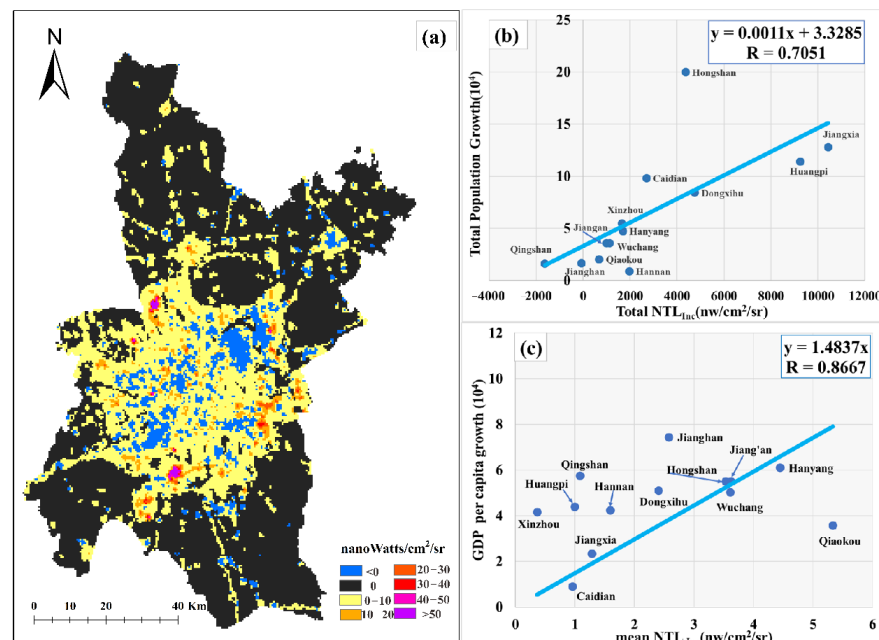


**Figure 9.** Dynamics NTL illumination in Wuhan during 2013–2018: (a) the increase of NTL radiance intensity during 2013–2018; (b) linear regression analysis between total population growth and total  $NTL_{Inc}$  at the district scale; (c) linear regression analysis between GDP growth per capita and mean  $NTL_{Inc}$  at the district scale.

#### 4.2. Identification of Urban Area Hotspots

Figure 10 shows the parameter optimization results of the SVM regression model in 2013. The grid search combined with five-fold CV serves as an effective strategy to optimize the parameters. As Figure 10 shows, the regression accuracy of  $C$  and  $\gamma$  in a specific range is very high, and the mean square error (MSE) of the fitted result in a specific range is very low. If the parameters were not selected properly, the accuracy would be too low. Therefore, we further narrowed the search range, and the values of  $C$  (1.6818) and  $\gamma$  (16384) with the highest accuracy were regarded as the best parameters for identifying the urban area hotspot in 2013. Subsequently, the optimal parameters for the other years (2015, 2018) were also acquired by following the above steps. After parameter optimization, the SVM regression model had good generalization ability for simulating the NTL intensity. In the study, all SVM regression models achieved good performance with a  $R^2 \approx 0.8$  in 2013, 2015, and 2018.

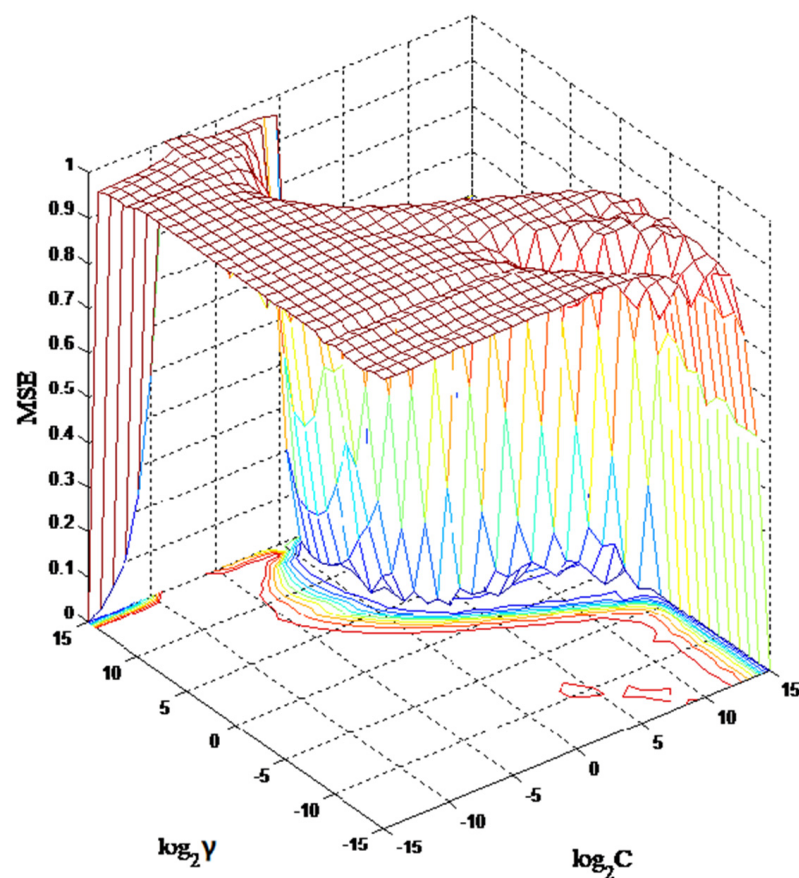
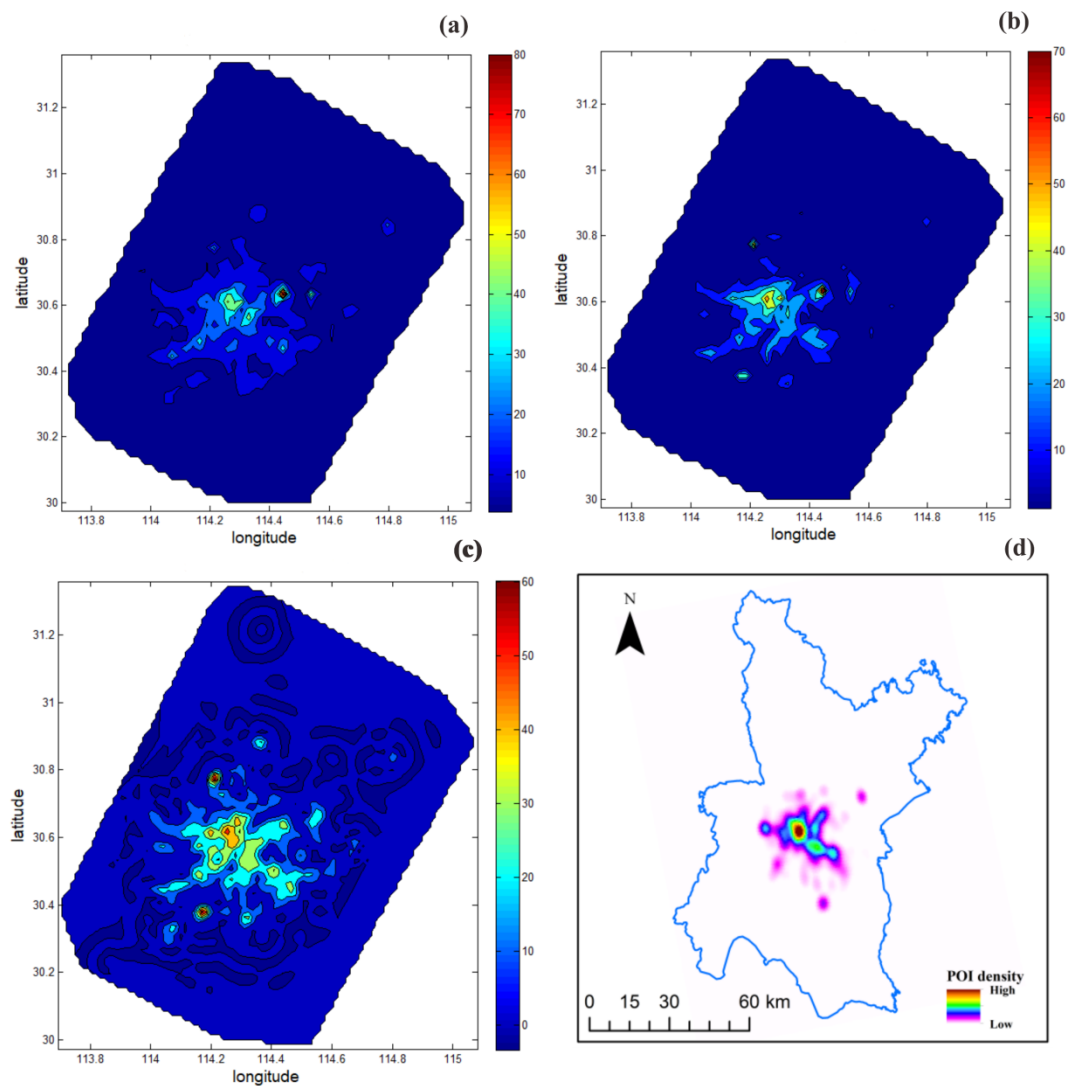


Figure 10. Parameter optimization of SVM regression model.

According to the simulated NTL intensity distribution, we can depict the urban area hotspots involving multiple bright pixels with high NTL intensity. Figure 11 shows the urban area hotspots from 2013 to 2018. The urban hotspots in 2013 (Figure 11a) were mainly concentrated in the Qingshan, Wuchang, and Jiang'an municipal districts. In 2015, the urban area hotspots expanded toward the southwest of Wuhan (Figure 11b). In 2018, the distribution of urban area hotspots was more balanced in the central area of Wuhan (Figure 11c), which is consistent with the distribution of POI density in 2018 (Figure 11d).



**Figure 11.** Urban area hotspots in Wuhan during 2013–2018 identified by SVM regression method: (a) urban area hotspots in 2013; (b) urban area hotspots in 2015; (c) urban area hotspots in 2018; (d) spatial distribution of POI density in 2018.

#### 4.3. Spatiotemporal Dynamic Analysis of Urban Area Hotspots

Table 2 shows the shift distance ( $L$ ) and angle ( $\alpha$ ) of the urban area hotspots' gravity center during the study period. The gravity center of urban area hotspots shifted to the southwest (SW) direction by 3.85 km from 2013 to 2015. Furthermore, the gravity center of urban area hotspots kept moving toward the SW direction by 2.76 km during 2015–2018.

**Table 2.** The moving distance  $L$  and angle  $\alpha$  of the center of gravity of urban area hotspots in Wuhan from 2013 to 2018.

Period	$L/\text{km}$	$\alpha/^\circ$
2013–2015	3.85	230.14
2015–2018	2.76	235.98

Figure 12a is a map of the gravity center of the urban area hotspots. According to the urban area extracted by the threshold value method based on annual stable VIIRS data of Wuhan from 2013 to 2018 (Figure 12b), we calculated the urban expansion intensity index (UEII) [55] in eight directions (N: north; NE: northeast; E: east; SE: southeast; S: south; SW: southwest; W: west; NW: northwest) during the time spans of 2013–2015 and 2015–2018. The results indicated that the centroid of urban areas of Wuhan also tends to move along a

SW direction, and the UEII was greater in 2013–2015 than in 2015–2018 according to the radar map of expanding intensity from 2013 to 2018 (Figure 12c). These comparisons reveal the consistency between the growth of urban area hotspots and urban expansion, which supports the validity of identification of urban area hotspots in this study.

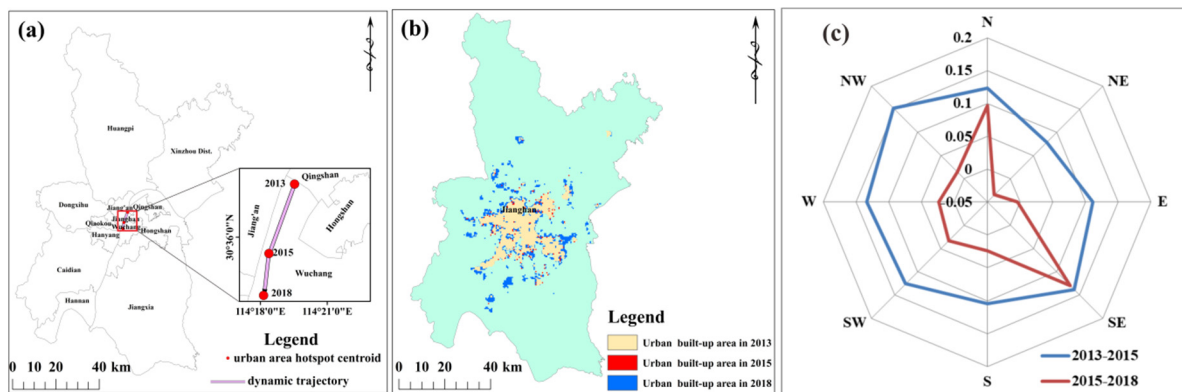


**Figure 12.** Consistency between the movement of urban area hotspots and urban expansion variation: (a) the movement of gravity center in Wuhan; (b) urban built-up area dynamics during 2013–2018; (c) expanding intensity of Wuhan from 2013 to 2018.

To some extent, the shift distance ( $L$ ) and angle ( $\alpha$ ) of the urban area hotspots' gravity center reveal the imbalance between different districts in Wuhan. During 2013–2018, the SW direction regions of Wuhan achieved more rapid development than other regions. On the one hand, it may be related to the prosperity of industrial parks located in southwest Wuhan, such as the Wuhan Economic and Technological Development Zone (EDZ) and the Dongxihu Development Zone (DDZ) [56]. On the other hand, the portion of the population from southwest districts of Wuhan kept increasing gradually during the study period [57]. Densely populated areas with intensified human activities tend to have higher nighttime light radiance, while rural areas tend to be dimly illuminated.

To further reveal the interaction between the spatiotemporal dynamics of urban hotspots and socioeconomic development related to human activities, we quantitatively explored the coupling between the movement of urban area hotspots and socioeconomic statistics indicators (i.e., population and GDP) during 2013–2018. Referring to the Wuhan statistical yearbooks, Figure 13 shows the movement of the population and GDP gravity center of Wuhan during 2013–2018. We utilized two metrics, the space-overlaps as  $S$  and changes in consistency as  $\theta$  [58], to quantify the coupling relationship.  $S$  measures the spatial distance between the two gravity centers in the same year. The farther the spatial distance, the lower the spatial coupling.  $\theta$  refers to the cosine of the angle between the vectors of the displacement of the two gravity centers relative to the previous time point. The range of  $\theta$  is  $[-1, 1]$ . When  $\theta$  is equal to 1, it means that the two gravity centers move in the same direction. While  $\theta$  is equal to  $-1$ , it means that the two gravity centers move in opposite directions. Therefore, we defined  $S_{u-p}$  and  $S_{u-G}$  to represent the space-overlaps between the moving trajectory of urban area hotspots and population gravity center, GDP, respectively. Meanwhile,  $\theta_{u-p}$  and  $\theta_{u-G}$  expressed changes in consistency between the moving trajectory of urban area hotspots and population gravity center, respectively.

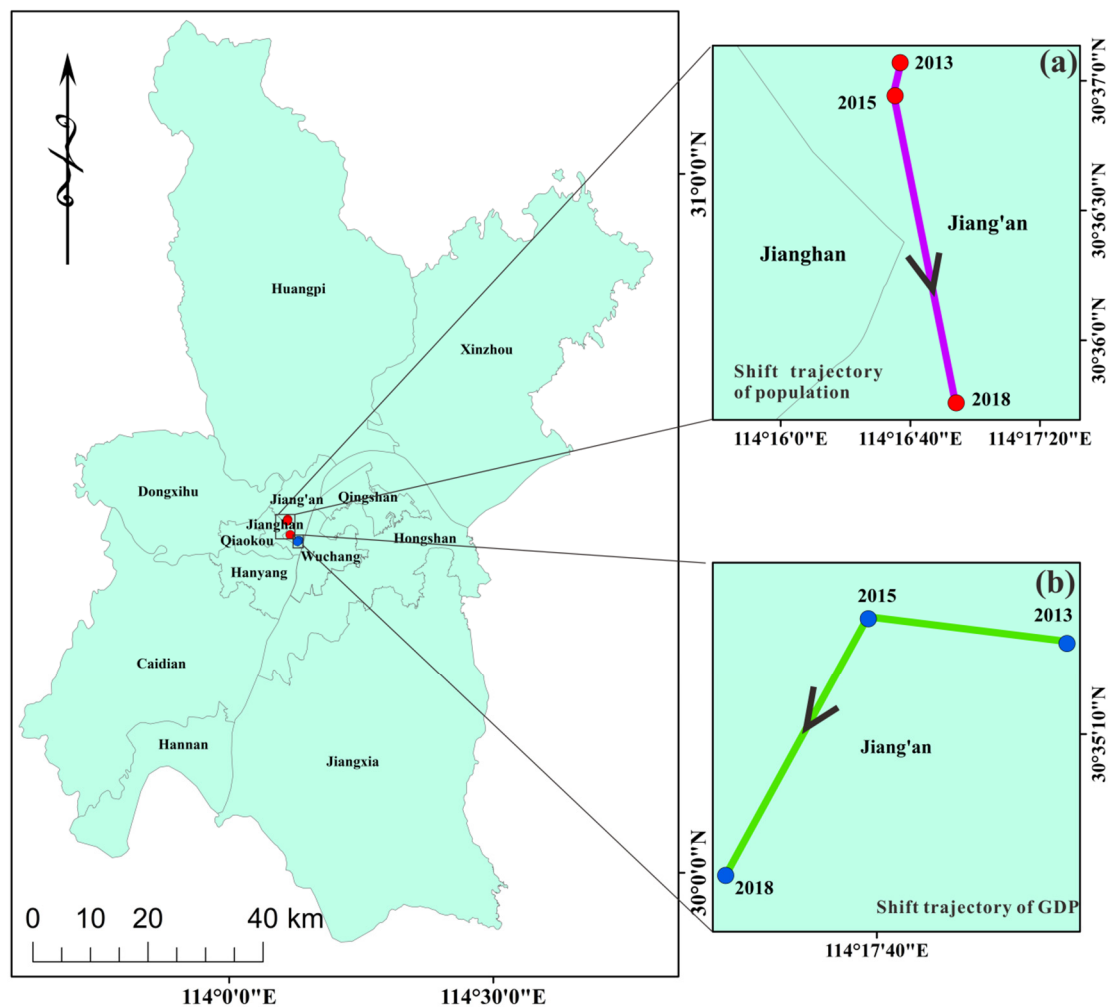


**Figure 13.** The shift trajectory of population and GDP gravity center of Wuhan during 2013–2018: (a) the shift trajectory of the population gravity center; (b) the shift trajectory of GDP gravity center.

Table 3 illustrates the  $S$  and  $\theta$  values in 2013, 2015, and 2018. During the study period, the higher  $\theta_{u-p}$  values revealed that the population had more influence on the increment of NTL intensity. With the development of urbanization, the  $\theta_{u-G}$  increased faster, indicating the growing effect of GDP on the formation of urban area hotspots. The decreasing  $S_{u-p}$  indicated that the effect of densely populated areas on the moving trajectory of urban area hotspots increased significantly. Moreover, the  $S_{u-G}$  first decreased and then rose, showing that the effect of GDP on the moving trajectory of urban area hotspot tended to rise first and then fall. In conclusion, the results manifest a good spatial coupling degree between urban area hotspots and socioeconomic development in Wuhan from 2013 to 2018.

**Table 3.** Space-overlaps ( $S$ ) and changes in consistency ( $\theta$ ) of city-level urban area hotspot and population and GDP gravity center.

Year	Urban Area Hotspot and Population		Urban Area Hotspot and GDP	
	$S_{u-p}$ (km)	$\theta_{u-p}$	$S_{u-G}$ (km)	$\theta_{u-G}$
2013	5.35	No data	5.99	No data
2015	4.6	0.90	1.64	0.43
2018	4.37	0.91	2.65	0.94

## 5. Discussion

NTL luminosity provides a unique opportunity to capture NTL clusters representing urban area hotspots closely related to human activities. Time-series nighttime images can be employed to monitor the spatiotemporal trajectory of urban area hotspots in a more direct and consistent fashion, compared to traditional census data. In this study, we proposed an applicable framework to monitor the spatiotemporal variation of urban area hotspots using VIIRS NTL images. Considering the existing phenomenon of NTL illumination seasonal variations, we employed the time-series analysis model to obtain the annual stable VIIRS data, and then the SVM regression method was used to identify urban NTL clusters. After parameter optimization by the grid search and K-CV techniques, nonlinear fitting with the SVM regression model presented a good ability to simulate urban area hotspots.

To validate the identification of urban area hotspots of Wuhan, we delineated the POIs kernel density map to recover the spatial distribution characteristics of urban area hotspots. By comparing the POIs map, the identified urban area hotspot well represented the inner urban spatial structure. Meanwhile, we compared the space-time trajectory of urban area hotspots with movement of the gravity center of urban areas extracted from the annual stable VIIRS data from 2013 to 2018. The results demonstrated the high consistency of direction of movement between the urban sprawl and urban area hotspot. The shift distance and angle of urban area hotspots' centroid further revealed the discrepancy of urban expansion during different periods, which will be beneficial to more sustainable urban planning and management. The coupling between the gravity center of the urban hotspot and socioeconomic statistics was analyzed for population and GDP. The results demonstrate that high GDP and dense population have a positive correlation with the increase of NTL intensity.

However, despite the merits of this study, a few data limitations should be mentioned. Firstly, existing NTL products (DMSP/OLS, VIIRS/DNB, LuoJia1-01, etc.) do not include the blue channel, and the increasing emission of blue light from LED sources may result in less total NTL emissions estimation. That is, VIIRS has a panchromatic band, making it incapable of measuring incoming light in the blue band, which may underestimate the total NTL emissions. Meanwhile, due to the unavailability of annual standard VIIRS products each year released by NOAA, we recognize the uncertainty of the annual stable VIIRS images obtained by time-series analysis method. Secondly, given that the population statistics represented the permanent resident population obtained from the statistical yearbook, the uncounted floating population and inaccurate statistics may affect the coupling relationship between the hotspot and the population. With the development of big data technology, it is possible to employ mobile internet data, such as mobile signaling [59], taxi-accessible tracks [60,61], check-in data in Sina web [62], and GPS data [63] as an effective reference for urban area hotspot categories. In a future study, we will explore urban area hotspot categories based on high-resolution NTL imagery combining more multi-source data.

Serving as a useful proxy for human activity, urban area hotspots reflect the spatial disparities among urban clusters due to urban expansion. A timely and explicit understanding of urban area hotspots is important for urban planning and environmental management. Due to the finer spatial and temporal resolution of VIIRS NTL imagery, the spatial distribution of NTL intensity surface may not always follow Gaussian surface exploited to simulate the urban hotspot from the DMSP NTL images [30]. Furthermore, the Gaussian volume model needs to treat each potential urban cluster separately, making the process of identifying urban area hotspots of polycentric cities more tedious. Referring to the UHI identification application, the SVM regression method is innovatively adopted for identification of urban area hotspots in this study. For irregular and complex spatial patterns of NTL intensity clusters distribution, the SVM regression method performs well as a fast, effective tool in simulating urban area hotspots, possessing good learning ability combined with grid search and k-fold CV techniques. Furthermore, we exhibited the diversified morphology of the urban area hotspots in the whole city over time. From the spatiotem-

poral analysis of urban area hotspots, we detected the coupling between the urban area hotspots and socioeconomic indicators (i.e., population and GDP). The finding shows the diversity of the urban NTL hotspots related to imbalanced human activities, although these statistical data may have some errors. This study could provide significant insights for decision-making analysis in urban development. Considering the urban expansion discrepancy and complexity of the hotspot migration in different polycentric cities, we will investigate the genericity and applicability of the whole method to other contexts in monitoring urban area hotspot migration in a future study.

## 6. Conclusions

This paper presents an innovative framework to identify urban area hotspots using VIIRS NTL images. Urban area hotspots were identified by the optimal SVM regression model combined with the grid search and k-fold cross-validation (K-CV) methods. A case study was used to depict the spatiotemporal dynamics of urban area hotspots within Wuhan during 2013–2018. The results confirm that the optimal SVM regression models successfully simulated urban area hotspots with a regression coefficient over 0.8. The results also prove that the proposed approach effectively depicts the location, spatial morphology, and migration trajectory of urban area hotspots, reflecting the explicit spatial variation of human activity with urban expansion.

Due to the rapid socioeconomic development and intensified human activity associated with urbanization, the spatiotemporal trajectory of urban area hotspots was consistent with the trend of urbanization development. This study explored the coupling between urban area hotspots and socioeconomic indicators (i.e., population and GDP). The results demonstrate that the relationship between the growth of urban hotspots and socioeconomic development manifests a high degree of spatial coupling. The NTL intensity increased in direct response to the increase of GDP and population. These findings prove that our proposed framework provides a novel perspective on the interaction between urban sprawl and human activities.

In future studies, the following issues should be considered: (1) the incorporation of more multi-source data to investigate urban area hotspots (such as cellular signaling data); (2) the possibility of urban area hotspot category identification based on high-resolution NTL imagery (such as LuoJia 1-01 data).

**Author Contributions:** Yanhong Zou, Minghui Chen and Yuling Ruan conceived and designed the study. Yanhong Zou, Yuling Ruan, and Jingya Shen collected and processed the data, performed the analysis, and wrote the paper. Minghui Chen contributed to data analysis and writing. Yanhong Zou and Yuling Ruan edited the draft, and approved the submitted manuscript. All authors have read and agreed to the published version of the manuscript.

**Funding:** This study was funded by the National Key R&D Program of China (2019YFC1805905), the National Natural Science Foundation of China (41872249) and the Fundamental Research Funds for the Central Universities of Central South University (2020zzts675).

**Institutional Review Board Statement:** Not applicable.

**Informed Consent Statement:** Not applicable.

**Data Availability Statement:** Data are private, available only for the review process of the present article by the ISPRS Int. J. Geo-Inf.

**Acknowledgments:** The authors would like to thank the editors and the reviewers for sharing their expert opinions on our manuscript, which has benefited from their constructive comments and suggestions.

**Conflicts of Interest:** The authors declare no conflict of interest.

## References

- Cohen, B. Urbanization in developing countries: Current trends, future projections, and key challenges for sustainability. *Technol. Soc.* **2006**, *28*, 63–80. [\[CrossRef\]](#)
- Montgomery, M. The Urban Transformation of the Developing World. *Science* **2008**, *319*, 761–764. [\[CrossRef\]](#)
- Ge, M.; Fang, S.; Gong, Y.; Tao, P.; Yang, G.; Gong, W. Understanding the Correlation between Landscape Pattern and Vertical Urban Volume by Time-Series Remote Sensing Data: A Case Study of Melbourne. *ISPRS Int. J. Geo-Inf.* **2021**, *10*, 14. [\[CrossRef\]](#)
- Ma, T.; Zhou, C.; Pei, T.; Haynie, S.; Fan, J. Quantitative estimation of urbanization dynamics using time series of DMSP/OLS nighttime light data: A comparative case study from China's cities. *Remote Sens. Environ.* **2012**, *124*, 99–107. [\[CrossRef\]](#)
- Zou, Y.; Peng, H.; Liu, G.; Yang, K.; Xie, Y.; Weng, Q. Monitoring Urban Clusters Expansion in the Middle Reaches of the Yangtze River, China, Using Time-Series Nighttime Light Images. *Remote Sens.* **2017**, *9*, 1007. [\[CrossRef\]](#)
- Zhou, Y.; Li, X.; Asrar, G.R.; Smith, S.J.; Imhoff, M. A global record of annual urban dynamics (1992–2013) from nighttime lights. *Remote Sens. Environ.* **2018**, *219*, 206–220. [\[CrossRef\]](#)
- Hu, X.; Qian, Y.; Pickett, S.; Zhou, W. Urban mapping needs up-to-date approaches to provide diverse perspectives of current urbanization: A novel attempt to map urban areas with nighttime light data. *Landsc. Urban Plan.* **2020**, *195*, 103709. [\[CrossRef\]](#)
- Jiang, S.; Wei, G.; Zhang, Z.; Wang, Y.; Xu, M.; Wang, Q.; Das, P.; Liu, B. Detecting the Dynamics of Urban Growth in Africa Using DMSP/OLS Nighttime Light Data. *Land* **2021**, *10*, 13. [\[CrossRef\]](#)
- Elvidge, C.; Baugh, K.E.; Kihn, E.; Kroehl, H.W.; Davis, E.R. Mapping city lights with nighttime data from the DMSP Operational Linescan System. *Photogramm. Eng. Remote Sens.* **1997**, *63*, 727–734.
- Amaral, S.; Câmara, G.; Monteiro, A.M.V.; Quintanilha, J.A.; Elvidge, C.D. Estimating population and energy consumption in Brazilian Amazonia using DMSP night-time satellite data. *Comput. Environ. Urban Syst.* **2005**, *29*, 179–195. [\[CrossRef\]](#)
- Hao, H.; Yu, D.; Liu, Y.; Sun, Y. Use of DMSP/OLS nighttime light data in urbanization monitor. *J. Beijing Norm. Univ. Nat. Sci.* **2014**, *50*, 407–413.
- Su, Y.; Chen, X.; Wang, C.; Zhang, H.; Liao, J.; Ye, Y.; Wang, C. A new method for extracting built-up urban areas using DMSP-OLS nighttime stable lights: A case study in the Pearl River Delta, southern China. *GIScience Remote Sens.* **2015**, *52*, 218–238. [\[CrossRef\]](#)
- Doll, C.H.; Muller, J.P.; Elvidge, C.D. Night-time Imagery as a Tool for Global Mapping of Socioeconomic Parameters and Greenhouse Gas Emissions. *AMBIO. A J. Hum. Environ.* **2000**, *29*, 157–162. [\[CrossRef\]](#)
- Shi, K.; Chen, Y.; Yu, B.; Xu, T.; Yang, C.; Li, L.; Huang, C.; Chen, Z.; Liu, R.; Wu, J. Detecting spatiotemporal dynamics of global electric power consumption using DMSP-OLS nighttime stable light data. *Appl. Energy* **2016**, *184*. [\[CrossRef\]](#)
- Ou, J.; Liu, X.; Li, X.; Li, M.; Li, W. Evaluation of NPP-VIIRS Nighttime Light Data for Mapping Global Fossil Fuel Combustion CO<sub>2</sub> Emissions: A Comparison with DMSP-OLS Nighttime Light Data. *PLoS ONE* **2015**, *10*, e0138310. [\[CrossRef\]](#) [\[PubMed\]](#)
- Levin, N.; Kyba, C.C.M.; Zhang, Q.; Sánchez de Miguel, A.; Román, M.O.; Li, X.; Portnov, B.A.; Molthan, A.L.; Jechow, A.; Miller, S.D.; et al. Remote sensing of night lights: A review and an outlook for the future. *Remote Sens. Environ.* **2020**, *237*, 111443. [\[CrossRef\]](#)
- Román, M.O.; Wang, Z.; Sun, Q.; Kalb, V.; Miller, S.D.; Molthan, A.; Schultz, L.; Bell, J.; Stokes, E.C.; Pandey, B.; et al. NASA's black marble nighttime lights product suite. *Remote Sens. Environ.* **2018**, *210*, 113–143. [\[CrossRef\]](#)
- Zhao, N.; Liu, Y.; Hsu, F.-C.; Samson, E.L.; Letu, H.; Liang, D.; Cao, G. Time series analysis of VIIRS-DNB nighttime lights imagery for change detection in urban areas: A case study of devastation in Puerto Rico from hurricanes Irma and Maria. *Appl. Geogr.* **2020**, *120*, 102222. [\[CrossRef\]](#)
- Bennett, M.M.; Smith, L.C. Advances in using multitemporal night-time lights satellite imagery to detect, estimate, and monitor socioeconomic dynamics. *Remote Sens. Environ.* **2017**, *192*, 176–197. [\[CrossRef\]](#)
- Wang, C.; Chen, Z.; Yang, C.; Li, Q.; Wu, Q.; Wu, J.; Zhang, G.; Yu, B. Analyzing parcel-level relationships between Luojia 1-01 nighttime light intensity and artificial surface features across Shanghai, China: A comparison with NPP-VIIRS data. *Int. J. Appl. Earth Obs. Geoinf.* **2020**, *85*, 101989. [\[CrossRef\]](#)
- Yu, B.; Tang, M.; Wu, Q.; Yang, C.; Deng, S.; Shi, K. Urban built-up area extraction from log-transformed NPP-VIIRS nighttime light composite data. *IEEE Geosci Remote Sens. Lett.* **2018**, *15*, 1279–1283. [\[CrossRef\]](#)
- Zheng, Q.; Weng, Q.; Wang, K. Developing a new cross-sensor calibration model for DMSP-OLS and Suomi-NPP VIIRS night-light imageries. *ISPRS J. Photogramm. Remote Sens.* **2019**, *153*, 36–47. [\[CrossRef\]](#)
- Li, X.; Levin, N.; Xie, J.; Li, D. Monitoring hourly night-time light by an unmanned aerial vehicle and its implications to satellite remote sensing. *Remote Sens. Environ.* **2020**, *247*, 111942. [\[CrossRef\]](#)
- Li, X.; Ma, R.; Zhang, Q.; Li, D.; Liu, S.; He, T.; Zhao, L. Anisotropic characteristic of artificial light at night—Systematic investigation with VIIRS DNB multi-temporal observations. *Remote Sens. Environ.* **2019**, *233*, 111357. [\[CrossRef\]](#)
- Zheng, Q.; Deng, J.; Jiang, R.; Wang, K.; Xue, X.; Lin, Y.; Huang, Z.; Shen, Z.; Li, J.; Amir, R.; et al. Monitoring and assessing “ghost cities” in Northeast China from the view of nighttime light remote sensing data. *Habitat Int.* **2017**, *70*. [\[CrossRef\]](#)
- Xie, Y.; Weng, Q.; Fu, P. Temporal variations of artificial nighttime lights and their implications for urbanization in the conterminous United States, 2013–2017. *Remote Sens. Environ.* **2019**, *225*, 160–174. [\[CrossRef\]](#)
- Li, S.; Cheng, L.; Liu, X.; Mao, J.; Wu, J.; Li, M. City type-oriented modeling electric power consumption in China using NPP-VIIRS nighttime stable light data. *Energy* **2019**, *189*, 116040. [\[CrossRef\]](#)
- Wu, B.; Yu, B.; Yao, S.; Wu, Q.; Chen, Z.; Wu, J. A surface network-based method for studying urban hierarchies by nighttime light remote sensing data. *Int. J. Geogr. Inf. Sci.* **2019**, *33*, 1377–1398. [\[CrossRef\]](#)

29. Lin, J.; Shi, W. Statistical Correlation between Monthly Electric Power Consumption and VIIRS Nighttime Light. *ISPRS Int. J. Geo-Inf.* **2020**, *9*, 32. [[CrossRef](#)]
30. Zheng, Q.; Jiang, R.; Wang, K.; Huang, L.; Ye, Z.; Gan, M.; Ji, B. Monitoring the trajectory of urban nighttime light hotspots using a Gaussian volume model. *Int. J. Appl. Earth Obs. Geoinf.* **2018**, *65*, 24–34. [[CrossRef](#)]
31. Xiao, P.; Wang, X.; Feng, X.; Zhang, X.; Yang, Y. Detecting China's Urban Expansion Over the Past Three Decades Using Nighttime Light Data. *IEEE J. Sel. Top. Appl. Earth Obs. Remote Sens.* **2014**, *7*, 4095–4106. [[CrossRef](#)]
32. Zhao, M.; Cheng, W.; Zhou, C.; Li, M.; Wang, N.; Liu, Q. Spatial differentiation and morphologic characteristics of China's urban core zones based on geomorphologic partition. *J. Appl. Remote Sens.* **2017**, *11*, 016041. [[CrossRef](#)]
33. Kyba, C.C.M. A proposed method for estimating regional and global changes in energy consumption for outdoor lighting. In Proceedings of the 5th International Conference on Artificial Light at Night, Salt Lake City, UT, USA, 12–14 November 2018.
34. Cai, J.; Huang, B.; Song, Y. Using multi-source geospatial big data to identify the structure of polycentric cities. *Remote Sens. Environ.* **2017**, *202*, 210–221. [[CrossRef](#)]
35. Qiu, Y.Q.; Xue, X.Y.; Han, W.J.; Chen, X.L.; Li, X. Comparison of Radiation Intensity and Estimation of Electric Power Consumption between DMSP/OLS and VIIRS Nighttime Light Images. *J. Appl. Sci.* **2019**, *37*, 99–111. [[CrossRef](#)]
36. Elvidge, C.; Baugh, K.; Zhizhin, M.; Hsu, F.-C. Why VIIRS data are superior to DMSP for mapping nighttime lights. *Proc. Asia-Pac. Adv. Netw.* **2013**, *35*, 62–69. [[CrossRef](#)]
37. Vapnik, V. *The Nature of Statistical Learning Theory*, 2nd ed.; Statistics for Engineering and Information Science; Springer: New York, NY, USA, 2000; p. 314. ISBN 0-387-98780-0.
38. Ahmad, S.; Kalra, A.; Stephen, H. Estimating soil moisture using remote sensing data: A machine learning approach. *Adv. Water Resour.* **2010**, *33*, 69–80. [[CrossRef](#)]
39. Luo, J.; Ming, D.; Shen, Z.; Wang, M.; Sheng, H. Multi-scale information extraction from high resolution remote sensing imagery and region partition methods based on GMRF-SVM. *Int. J. Remote Sens.* **2007**, *28*, 3395–3412. [[CrossRef](#)]
40. Kumar, P.; Gupta, D.K.; Mishra, V.; Prasad, R. Comparison of support vector machine, artificial neural network, and spectral angle mapper algorithms for crop classification using LISS IV data. *Int. J. Remote Sens.* **2015**, *36*, 1604–1617. [[CrossRef](#)]
41. Guo, W.; Xia, X.; Xiaofei, W. A remote sensing ship recognition method based on dynamic probability generative model. *Expert Syst. Appl.* **2014**, *41*, 6446–6458. [[CrossRef](#)]
42. Yuan, H.; Yang, G.; Li, C.; Wang, Y.; Liu, J.; Yu, H.; Feng, H.; Xu, B.; Zhao, X.; Yang, X. Retrieving Soybean Leaf Area Index from Unmanned Aerial Vehicle Hyperspectral Remote Sensing: Analysis of RF, ANN, and SVM Regression Models. *Remote Sens.* **2017**, *9*, 309. [[CrossRef](#)]
43. Zhan, W.; Chen, Y.; Zhou, J.; Li, J. Spatial simulation of Urban Heat Island intensity based on the support vector machine technique: A case study in Beijing. *Acta Geod. Et Cartogr. Sin.* **2011**, *40*, 96–103.
44. Yang, H.; Meng, N.; Wang, J.; Zheng, Y.; Zhao, L. Spatial-temporal morphology simulation of Beijing-Tianjin-Hebei urban agglomeration thermal environment based on Support Vector Machine. *J. Geo-Inf. Sci.* **2019**, *21*, 190–200.
45. Savitzky, A.; Golay, M. Smoothing and differentiation of data by simplified least squares procedures. *Anal. Chem.* **1964**, *36*, 1627–1639. [[CrossRef](#)]
46. Chen, J.; Jönsson, P.; Tamura, M.; Gu, Z.; Matsushita, B.; Eklundh, L. A simple method for reconstructing a high-quality NDVI time-series data set based on the Savitzky–Golay filter. *Remote Sens. Environ.* **2004**, *91*, 332–344. [[CrossRef](#)]
47. Jönsson, P.; Eklundh, L. TIMESAT—A program for analyzing time-series of satellite sensor data. *Comput. Geosci.* **2004**, *30*, 833–845. [[CrossRef](#)]
48. Levin, N. The impact of seasonal changes on observed nighttime brightness from 2014 to 2015 monthly VIIRS DNB composites. *Remote Sens. Environ.* **2017**, *193*, 150–164. [[CrossRef](#)]
49. Chen, Z.; Yu, B.; Ta, N.; Shi, K.; Yang, C.; Wang, C.; Zhao, X.; Deng, S.; Wu, J. Delineating Seasonal Relationships Between Suomi NPP-VIIRS Nighttime Light and Human Activity Across Shanghai, China. *IEEE J. Sel. Top. Appl. Earth Obs. Remote Sens.* **2019**, *12*, 4275–4283. [[CrossRef](#)]
50. Zhang, Z.; Sun, T.; Xie, X.; Chen, C.; Lv, X. Early auxiliary screening of cerebral infarction based on lacrimal Raman spectroscopy and SVM algorithm. *Optik* **2020**, *218*, 165248. [[CrossRef](#)]
51. Ding, S.; Qi, B.; Tan, H. An overview on theory and algorithm of support vector machines. *J. Univ. Electron. Sci. Technol. China* **2011**, *40*, 2–10. [[CrossRef](#)]
52. Ring, M.; Eskofier, B.M. An approximation of the Gaussian RBF kernel for efficient classification with SVMs. *Pattern Recognit. Lett.* **2016**, *84*, 107–113. [[CrossRef](#)]
53. Chen, H.; Liu, Z.; Cai, K.; Xu, L.; Chen, A. Grid search parametric optimization for FT-NIR quantitative analysis of solid soluble content in strawberry samples. *Vib. Spectrosc.* **2018**, *94*, 7–15. [[CrossRef](#)]
54. Zhao, H.; Shao, S.; Xie, D. Examination method for outlier of analytical data. *J. Zhoukou Teach. Coll.* **2004**, *21*, 70–72.
55. Xie, Y.; Wei, X.; Sun, X. Analysis on the Characteristics and Spatial Pattern of Urban Expansion in Nanchang. *Jiangxi Sci.* **2020**, *38*, 662–672.
56. Shao, Q.; Fan, T. Economic Development Factors Analysis of Airport Economic Zone—Evidence from Wuhan Airport Economic Development Zone. *Econ. Res. Guide* **2014**, *24*, 66–68.
57. Wuhan Statistics Bureau. *Wuhan Statistical Yearbook*; Beijing China Statistics Press: Beijing, China, 2019.

58. Gao, J.; Xie, W.; Han, Y.; Zhang, Y.; Chen, J. The Evolutionary Trend and the Coupling Relation of Gravity Center Moving of County-level Population Distribution, Economical Development and Grain Production During 1990–2013 in Henan Province. *Sci. Geogr. Sin.* **2018**, *38*, 919–926.
59. Xu, J.; Fang, Z.; Xiao, S.; Yin, L. The Spatio-temporal Heterogeneity Analysis of Massive Urban Mobile Phone Users' Stay Behavior: A Case Study of Shenzhen City. *J. Geoinf. Sci.* **2015**, *17*, 197–205.
60. Liu, Y.; Wang, F.; Xiao, Y.; Gao, S. Urban land uses and traffic 'source-sink areas': Evidence from GPS-enabled taxi data in Shanghai. *Landscape Urban Plan.* **2012**, *106*, 73–87. [[CrossRef](#)]
61. Zhang, P.; Deng, M.; Shi, Y.; Zhao, L. Detecting hotspots of urban residents' behaviours based on spatio-temporal clustering techniques. *GeoJournal* **2017**, *82*, 923–935. [[CrossRef](#)]
62. Wang, B.; Zhen, F.; Zhang, H. The dynamic changes of urban space-time activity and activity zoning based on check-in data in Sina web. *Sci. Geogr. Sin.* **2015**, *35*, 151–160. [[CrossRef](#)]
63. Chen, S.; Tao, H.; Li, X.; Zhuo, L. Discovering urban functional regions using latent semantic information: Spatiotemporal data mining of floating cars GPS data of Guangzhou. *Acta Geogr. Sin.* **2016**, *71*, 471–483. [[CrossRef](#)]